



Excitation-dependent features and artifacts in 2-D terahertz spectroscopy

ALBERT LIU^{1,*}  AND ANKIT DISA² 

¹*Condensed Matter Physics and Materials Science Division, Brookhaven National Laboratory, Upton, New York 11973, USA*

²*School of Applied & Engineering Physics, Cornell University, Ithaca, New York 14853, USA*

**aliu1@bnl.gov*

Abstract: Recently, two-dimensional terahertz spectroscopy (2DTS) has attracted increasing attention for studying complex solids. A number of recent studies have applied 2DTS either with long pulses or away from any material resonances, situations that yield unconventional 2DTS spectra that are often difficult to interpret. Here, we clarify the generic origins of observed spectral features by examining 2DTS spectra of ZnTe, a model system with a featureless optical susceptibility at low terahertz frequencies. These results also reveal possible artifacts that may arise from electro-optic sampling in collinear 2DTS experiments, including the observation of spurious rectified or second harmonic signals.

© 2024 Optica Publishing Group under the terms of the [Optica Open Access Publishing Agreement](#)

1. Introduction

Two-dimensional optical spectroscopy [1,2] and its predecessor, two-dimensional nuclear magnetic resonance (NMR) [3], are powerful techniques that have found widespread use, in both industrial application and fundamental science. Recently, advances in laser technology have extended these multi-dimensional spectroscopies into terahertz frequencies in which many fundamental excitations of condensed matter are found. So-called 2-D THz spectroscopy (2DTS) [4–6] has been demonstrated in a variety of material systems, such as molecular gases [7,8], semiconductors [9–12], ferroics [13–16], superconductors [17–19], and even topological materials [20].

Two-dimensional optical spectroscopy and two-dimensional NMR are most often performed and interpreted in the impulsive limit [21,22], in which the measured nonlinear wave-mixing signal directly reflects a microscopic optical response function with only a scalar dependence on the excitation field amplitudes E_A and E_B [23]. As shown in Fig. 1(a), in the time-domain, this limit corresponds to excitation pulse durations far shorter than any relevant dephasing times, while in the frequency-domain, this limit corresponds to an excitation bandwidth far broader than the spectral content of the relevant optical response function.

These conditions, however, are increasingly violated in 2DTS experiments, due to both limitations of terahertz light sources and the relevance of low-energy continua in the physics of solid-state materials. For example, as shown in Fig. 1(b), excitation pulse durations may be comparable to system dephasing times which corresponds to excitation spectral bandwidths comparable or greater than resonance linewidths. In addition, as shown in Fig. 1(c), the excitation bandwidth may not be centered on any resonance, probing only a featureless continuum. Though distinct in origin, these two cases both result in a nonlinear signal that is generated only during pulse overlap and a two-dimensional spectrum that is shaped primarily by the excitation pulse spectrum.

Here, we aim to clarify the generic spectral features of non-resonant (and non-impulsive) 2DTS experiments. We present 2DTS spectra of ZnTe, a model system with a featureless optical susceptibility in the few-THz frequency regime, which exhibit characteristic features due to both second- and third-order optical nonlinearities that are well-reproduced by simulation. As will be

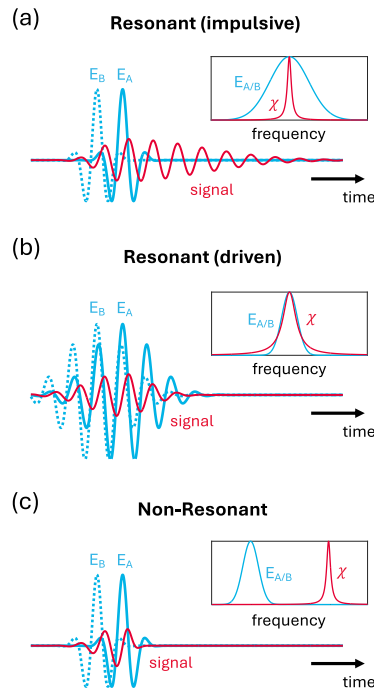


Fig. 1. Three regimes of nonlinear signal generation by two excitation pulses E_A and E_B in 2DTS. (a) Impulsive excitation of a resonance χ , in which excitation pulse durations are far shorter than relevant dephasing times. (b) Driven excitation of the resonance, in which pulse durations are comparable to relevant dephasing times. (c) Off-resonant excitation, in which the excitation spectrum does not overlap with any material resonance. Insets depict corresponding spectral overlap of the excitation spectra $E_{A/B}$ and optical response χ .

elucidated below, these results also reveal artifacts that may arise in 2DTS experiments due to a collinear detection setup.

2. Experimental details

Figure 2(a) illustrates our experimental setup, which emulates a typical 2TDS experiment in a reflection geometry. Two terahertz pulses E_A and E_B are generated by optical rectification in two separate organic crystals DAST [24] (at a 1 kHz repetition rate), which are combined collinearly using an initial silicon beamsplitter. These pulses then propagate through a second silicon beamsplitter to the sample position, and their subsequent reflections then propagate to the electro-optic sampling (EOS) position where they are combined with an 800 nm probe pulse on a ZnTe crystal of 150 μm thickness. Although electro-optic sampling in this experiment was not calibrated to the absolute electric field, we estimate peak fields on the order of tens of kV/cm per pulse (where $E_A \approx 3E_B$). In the usual case, the ZnTe would act as an EOS detector for the nonlinear signal generated by the mixing of E_A and E_B at the sample position, but here we examine the characteristic 2TDS responses of the ZnTe itself to the non-resonant excitation from the incident fields.

ZnTe exhibits a relatively featureless optical susceptibility at frequencies below its first optical phonon resonance at 5.3 THz [25]. This resonance lies above the spectra of the excitation pulses $E_{A/B}$, as shown in the inset of Fig. 2(a), leading to a non-resonant excitation condition (as shown

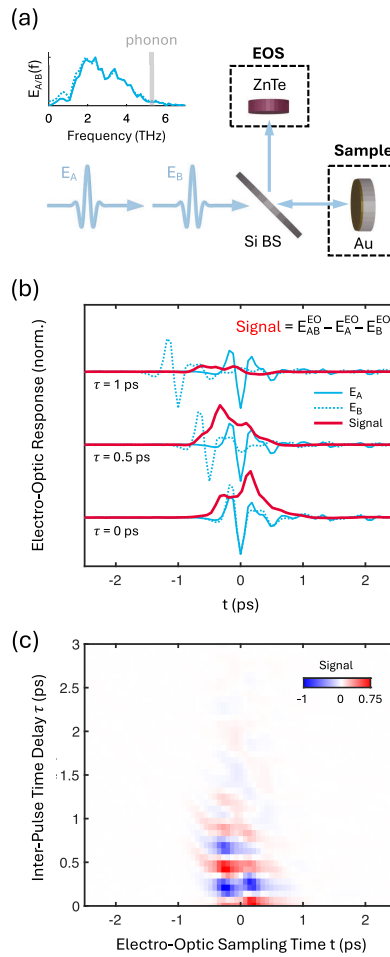


Fig. 2. (a) 2DTS experiment in a reflection geometry, with a gold mirror placed at the sample position. The normalized excitation spectra $E_{A/B}(f)$, measured with a separate GaP EOS detector and shown inset, are largely below the lowest phonon resonance of ZnTe at 5.3 THz. (b) Excitation fields $E_{A/B}$ (normalized to their respective peak fields) plotted alongside the non-resonant nonlinear signal (normalized to the peak signal field at $\tau = 0$) for three time delays as indicated. (c) Two-dimensional time profile of the nonlinear signal as a function of inter-pulse time delay τ and laboratory time t .

in Fig. 1(c)). To examine this situation, we therefore place a gold mirror at the sample position so that the primary nonlinearity driven by E_A and E_B is that of the ZnTe electro-optic crystal itself. A standard double-chopping scheme is used in which pulses A and B are modulated at 1/2 kHz and 1/3 kHz respectively, resulting in a nonlinear signal that can be lock-in detected at 1/6 kHz. The nonlinear signal is then defined by

$$\text{Signal} = E_{AB}^{EO} - E_A^{EO} - E_B^{EO}, \quad (1)$$

where E_{AB}^{EO} represents the electro-optic response when both excitation pulses are present, and E_A^{EO} and E_B^{EO} are the electro-optic responses with each pulse present individually.

In Fig. 2(b), the time profiles of both excitation pulses and the generated nonlinear signal are shown for three inter-pulse time delays $\tau = 0, 0.5, \text{ and } 1$ ps. We now point out two salient features of these measurements. First, a nonlinear signal is generated only when the two excitation pulses are overlapping in time, and it moves backwards in time with the overlap region as τ increases. Second, the time profile of the nonlinear signal at the delays shown is clearly unipolar, which reflects rectification arising from a second-order coordinate response of the ZnTe [26]. We remark that this signal is clearly not a radiated field, but is essentially the electro-optic Kerr effect [27] driven by two distinct excitation fields. The full two-dimensional time evolution of the nonlinear signal is shown in Fig. 2(c), which primarily exhibits the unipolar signal at early delays τ and an interesting sub-structure beyond $\tau = 1$ ps.

3. Phenomenological model

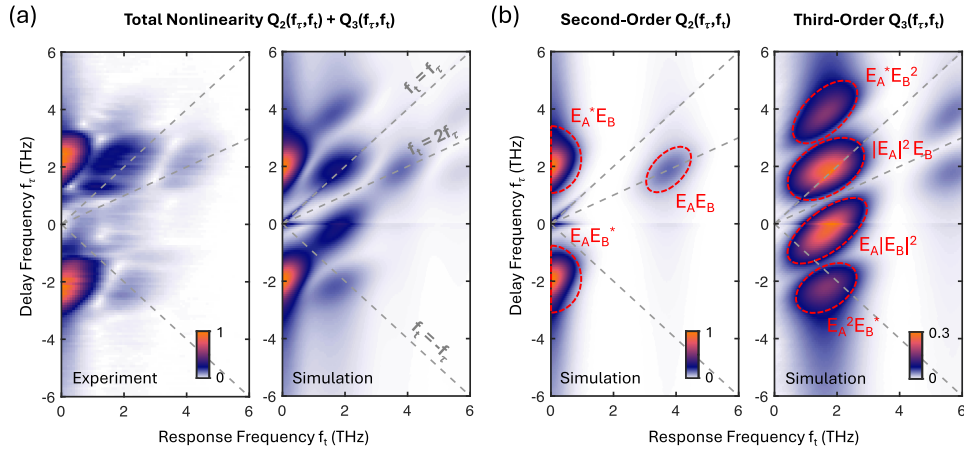


Fig. 3. (a) Comparison of the experimental 2DTS spectrum of ZnTe and a corresponding spectrum simulated as described in the text. Both are acquired in an off-resonant excitation condition and normalized to their maximum values. (b) Spectra of solely the second-order and third-order coordinate responses (normalized to the peak value of Q_2) as indicated, which correspond to the electro-optic Kerr effect and fourth-order electro-optic effect respectively. Each peak is labeled by its underlying wave-mixing term.

To understand the complex dynamics exhibited in Fig. 2(c), we Fourier transform along both time axes $\{\tau, t\}$, obtaining a two-dimensional spectrum. The resultant spectrum is shown in the left panel of Fig. 3(a), which exhibits multiple peaks that correspond to distinct electro-optic nonlinearities of the ZnTe.

The origin of each feature can be understood by considering a simple model in which a nonlinear oscillator (e.g. a phonon) is driven (in this case, non-resonantly) by the electric field

$E(t)$. The total energy of such a system can be written as:

$$H = H_K + H_U + H_{L-M} \quad (2)$$

where we have a kinetic energy, $H_K = \frac{1}{2}m \left(\frac{dQ}{dt}\right)^2$, and a light-matter coupling term $H_{L-M} = -z^*QE(t)$ where Q is the oscillator coordinate, z^* is its effective charge, and m its effective mass. The potential energy H_U contains a harmonic term with a natural frequency ω_0 in addition to anharmonic contributions. Since ZnTe lacks inversion symmetry, we include both cubic and quartic anharmonicities:

$$H_U = \frac{1}{2}m\omega_0^2Q^2 + \frac{1}{3}maQ^3 + \frac{1}{4}mbQ^4 \quad (3)$$

For $b>0$, the potential stiffens with increasing excursions of Q and is therefore the usual case to satisfy stability criteria.

The equation of motion for $Q(t)$ is given by:

$$\begin{aligned} \frac{d^2Q}{dt^2} &= -\frac{1}{m} \frac{\partial H}{\partial Q} - \gamma \frac{dQ}{dt} \\ &= -\omega_0^2Q - aQ^2 - bQ^3 + \frac{z^*}{m}E(t) - \gamma \frac{dQ}{dt}, \end{aligned} \quad (4)$$

where we've also included a phenomenological damping term with a damping rate γ . The above equation may be solved perturbatively by assuming an ansatz for $Q(t)$ as a power series in λ , a dummy variable that we can set to unity at the end of our analysis:

$$Q(t) = \lambda Q_1(t) + \lambda^2 Q_2(t) + \lambda^3 Q_3(t) + \dots \quad (5)$$

Plugging this solution into (4) and collecting terms in powers of λ , we obtain a hierarchy of equations:

$$\ddot{Q}_1 = -\omega_0^2 Q_1 - \gamma \dot{Q}_1 + \frac{z^*}{m} E(t) \quad (6a)$$

$$\ddot{Q}_2 = -\omega_0^2 Q_2 - \gamma \dot{Q}_2 - aQ_1^2 \quad (6b)$$

$$\ddot{Q}_3 = -\omega_0^2 Q_3 - \gamma \dot{Q}_3 - 2aQ_1Q_2 - bQ_1^3 \quad (6c)$$

\vdots

Note that, from the simple cubic and quartic nonlinearities in H_U , a cascade of nonlinearities follow to infinite order. The corrections $Q_n(t)$ decrease in magnitude with increasing order n , so we truncate our solution at $Q_3(t)$.

Equations (6) provide an intuitive picture for the nonlinear dynamics upon driving. Equation (6a) for $Q_1(t)$ describes a harmonic oscillator of resonance frequency ω_0 driven by $E(t)$, and therefore corresponds to solely the linear response of $Q(t)$. Equations (6b) and (6c) then each describe a harmonic oscillator of identical resonance frequency ω_0 but driven indirectly by $-aQ_1^2$ and $-2aQ_1Q_2 - bQ_1^3$ respectively. The nonlinear signal is then determined by a combination of $Q_2(t)$ and $Q_3(t)$, and in principle higher-order contributions that are assumed to be negligible.

We now numerically solve the above system of equations for $\{Q_1, Q_2, Q_3\}$ with a standard Runge-Kutta solver method. In the simulations, the system is excited by two identical ($E_A = E_B$) pulses

$$E(t) = E_A e^{-t^2/2\sigma_t^2} e^{i\omega_c t} + E_B e^{-(t+\tau)^2/2\sigma_t^2} e^{i\omega_c(t+\tau)} + \text{c.c.} \quad (7)$$

of carrier frequency $\omega_c = 2$ THz and pulse duration $\sigma_t = 400$ fs that resemble the experimental pulse spectra. To simulate the non-resonant excitation condition, the oscillator frequency is set

to the transverse-optical phonon frequency of ZnTe with $\omega_0 = 5.3$ THz, and a large damping rate of $\gamma = 285$ THz to preclude any resonant effects. The nonlinear coefficients (a and b) were fit to match the relative peak intensities observed in our experiment. For simplicity, we neglect modes at higher frequency since they contribute weaker nonlinear responses and would produce qualitatively similar 2DTS spectra. The result of simulating the total nonlinearity $Q_2 + Q_3$ is shown in the right panel of Fig. 3(a), which reproduces nearly all of the salient peak positions and lineshapes of the experimental spectrum.

We can further clarify the origins of each peak by plotting the second- and third-order coordinate responses individually, which are shown in Fig. 3(b). To then identify the underlying wave-mixing combinations, we can analyze the equations of motion heuristically by noting that Q_1 will yield a general solution of the form:

$$Q_1 = Q_1^A [E_A e^{i\omega_c t} + E_A^* e^{-i\omega_c t}] + Q_1^B [E_B e^{i\omega_c(t+\tau)} + E_B^* e^{-i\omega_c(t+\tau)}] \quad (8)$$

where the oscillation frequency is set to ω_c due to the non-resonant excitation condition and the response amplitudes and oscillation phases are combined into the prefactors $Q_1^{A/B}$. The forcing function (dropping the terms proportional to $(Q_1^A)^2$ and $(Q_1^B)^2$ which are filtered by the detection scheme in Eq. (1)) for Q_2 is then directly found as $-aQ_1^2 = -aQ_1^A Q_1^B (E_A E_B e^{i\omega_c(2t+\tau)} + E_A E_B^* e^{-i\omega_c \tau} + \text{c.c.})$, giving a general solution:

$$Q_2 = Q_2^{AB} [E_A E_B e^{i\omega_c(2t+\tau)} + E_A E_B^* e^{-i\omega_c \tau} + \text{c.c.}] \quad (9)$$

where relevant prefactors have once again been combined into Q_2^{AB} . We may now directly read the oscillation frequencies in each phase factor to determine their respective coordinates in a two-dimensional spectrum, which are $\{f_i, f_\tau\} = \{2\omega_c, \omega_c\}$ and $\{f_i, f_\tau\} = \{0, -\omega_c\}$ for the first and second terms respectively. Performing the same procedure for Q_3 , we find:

$$Q_{NL} \propto Q_3^{A|B|^2} E_A |E_B|^2 e^{i\omega_c t} + Q_3^{A^* BB} E_A^* E_B^2 e^{i\omega_c(t+2\tau)} + Q_3^{|A|^2 B} |E_A|^2 E_B e^{i\omega_c(t+\tau)} + Q_3^{AAB^*} E_A^2 E_B^* e^{i\omega_c(t-\tau)} + Q_3^{ABB} E_A E_B^2 e^{i\omega_c(3t+2\tau)} + Q_3^{AAB} E_A^2 E_B e^{i\omega_c(3t+\tau)} + \text{c.c.} \quad (10)$$

where we can likewise read the frequency coordinates, which have been labeled in Fig. 3(b). Again, nonlinearities that scale with only a single excitation pulse are dropped due to the detection scheme in Eq. (1). We note that the peaks located at $\{f_i, f_\tau\} = \{2, 4\}$ THz and $\{2, 0\}$ THz are not pronounced in the experimental spectra due to the lower peak field of E_B with respect to that of E_A , as confirmed by simulations performed with unbalanced pulse amplitudes.

4. Discussion

The model presented above matches the experimental spectra well, showing the unique features of non-resonantly driven nonlinear systems. With this understanding, we now show that equivalent features can also arise from non-impulsive, resonantly driven systems (i.e. when the incident THz field bandwidths are on the order of or greater than that of the oscillator). In Fig. 4(a) we show the familiar resonant spectra observed in the impulsive limit, simulated with the same parameters as in Fig. 3, but with a hypothetical mode at $\omega_0 = 2$ THz and $\gamma = 1$ THz. These spectra exhibit symmetric lineshapes along both axes f_τ and f_i , and is therefore what we would qualitatively expect from resonantly exciting the ZnTe phonon mode with an excitation bandwidth

that exceeds the phonon linewidth. In Fig. 4(b), the damping rate is increased to $\gamma = 10$ THz to exceed the excitation spectral bandwidth (FWHM ≈ 1 THz), resulting in a nonlinear signal generated solely during temporal overlap of the excitation pulses. The spectra in Fig. 4(b) bear a remarkable resemblance to the non-resonant spectra shown in Fig. 3(b), since in both cases the nonlinear response is predominately shaped by the excitation spectrum.

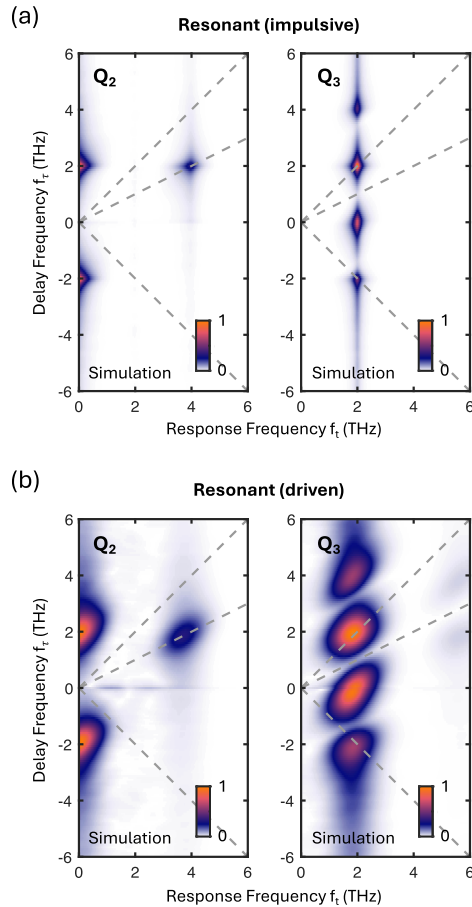


Fig. 4. Simulated 2DTS spectra under resonant driving ($\omega_0 = \omega_c = 2$ THz) in the (a) impulsive limit ($\gamma = 1$ THz) and (b) driven limit ($\gamma = 10$ THz). In the impulsive limit, symmetric peak lineshapes are observed that resemble those from conventional multidimensional spectra, while in the driven limit the spectra resemble the non-resonant spectra presented in Fig. 3.

Indeed, a distinctive feature of the spectra in Fig. 3(b) and Fig. 4(c) are their asymmetric lineshapes, as all peaks exhibit a marked elongation along the $f_\tau = f_i$ direction (from the origin to the upper right corner). This may be understood by considering the fact that the temporal overlap of the pulses, during which a non-resonant (or non-impulsive) nonlinear signal is generated, moves backwards in time as the inter-pulse time delay τ increases (which can be seen for example in Fig. 2). The frequency-domain representation of such a non-resonant signal along $t = -\tau$ may be most easily intuited by comparison to a photon echo signal along $t = \tau$, which results in the inverse spectral lineshape along $f_\tau = -f_i$.

As noted above, the experimental setup used here is deliberately generic. Replacing the gold mirror in Fig. 2(a) with any material of interest results in a typical collinear 2DTS experiment,

measured in reflection. In such an experiment, ideally one only measures the emitted nonlinear signal ($E_{AB}^{EO} - E_A^{EO} - E_B^{EO}$) generated from the mixing of E_A and E_B in the sample. If only the nonlinear signal is present in the EOS crystal (e.g. ZnTe), one can measure its field profile in time through the standard linear electro-optic (Pockels) effect. The results presented here, though, reveal possible artifacts (similar to the well-known ‘coherent artifacts’ in transient absorption spectroscopy [28]) that may arise in such a geometry in which, in addition to the nonlinear signal, both excitation pulses, E_A and E_B reflect off the sample and reach the EOS crystal. Therefore, even with a double-chopping scheme, a non-resonant nonlinearity of the form presented here may be observed in the signal from the EOS crystal, in addition to the material response of interest. Care must therefore be taken in collinear experiments to verify the absence of rectified nonlinearities that scale as $E_A^* E_B$ or $E_A E_B^*$, which are the leading terms in the quadratic electro-optic nonlinearity from the EOS crystal. These terms lead to responses at zero frequency and, thus, should not radiate from a probed sample. Such zero frequency signals present in the measured nonlinear response are, therefore, artifacts of the detection scheme in a collinear geometry, which may occur in both reflection and transmission configurations.

Distinguishing third-order artifacts from a true sample signal may be less obvious however, in which case additional measurements may be performed to check the source of a nonlinearity. For example, one can verify that the electro-optic response scales linearly with signal field and shows a theoretically expected polarization dependence by adding an analyzer between the sample and the EOS detection (as exemplified by Refs. [15,16]). In certain cases however, nonlinear excitation of the EOS detector may be unavoidable due to weak signal strength with respect to excitation field. To avoid nonlinear excitation of the EOS crystal entirely, one can implement a non-collinear geometry, in which only the nonlinear electric field from the sample is able to reach the EOS crystal [18].

5. Conclusion

In conclusion, we have performed two-dimensional terahertz spectroscopy in a non-resonant excitation condition on ZnTe. The resultant spectrum exhibits unique features and lineshapes that are reproduced well by a simple simulation. We also present a perturbative analysis of the equations of motion to assign wave-mixing terms to each observed peak, and point out the lineshape elongation that may be used as indication of a spectrum taken in either a driven or non-resonant excitation condition. Finally, our results reveal potential nonlinear electro-optic artifacts that may contaminate spectra taken in collinear experimental geometries.

Funding. U.S. Department of Energy (DE-SC0012704).

Acknowledgments. The authors are grateful to Keith Nelson and Zhuquan Zhang for fruitful discussions. A.L. was supported by the U.S. Department of Energy, Office of Basic Energy Sciences, under Contract No. DE-SC0012704.

Disclosures. The authors declare no conflicts of interest.

Data availability. Data underlying the results presented in this paper are not publicly available at this time but may be obtained from the authors upon reasonable request.

References

1. S. T. Cundiff and S. Mukamel, “Optical multidimensional coherent spectroscopy,” *Phys. Today* **66**(7), 44–49 (2013).
2. H. Li, B. Lomsadze, G. Moody, *et al.*, *Optical Multidimensional Coherent Spectroscopy* (Oxford University Press, 2023).
3. R. Ernst, G. Bodenhausen, and A. Wokaun, *Principles of Nuclear Magnetic Resonance in One and Two Dimensions*, International series of monographs on chemistry (Clarendon Press, 1990).
4. C. L. Johnson, B. E. Knighton, and J. A. Johnson, “Distinguishing nonlinear terahertz excitation pathways with two-dimensional spectroscopy,” *Phys. Rev. Lett.* **122**(7), 073901 (2019).
5. J. Lu, X. Li, Y. Zhang, *et al.*, *Two-Dimensional Spectroscopy at Terahertz Frequencies* (Springer International Publishing, 2019), pp. 275–320.
6. K. Reimann, M. Woerner, and T. Elsaesser, “Two-dimensional terahertz spectroscopy of condensed-phase molecular systems,” *J. Chem. Phys.* **154**(12), 120901 (2021).

7. J. Lu, Y. Zhang, H. Y. Hwang, *et al.*, “Nonlinear two-dimensional terahertz photon echo and rotational spectroscopy in the gas phase,” *Proc. Natl. Acad. Sci.* **113**(42), 11800–11805 (2016).
8. F. Y. Gao, Z. Zhang, Z.-J. Liu, *et al.*, “High-speed two-dimensional terahertz spectroscopy with echelon-based shot-to-shot balanced detection,” *Opt. Lett.* **47**(14), 3479–3482 (2022).
9. T. Maag, A. Bayer, S. Baiertl, *et al.*, “Coherent cyclotron motion beyond Kohn’s theorem,” *Nat. Phys.* **12**(2), 119–123 (2016).
10. C. Somma, G. Følpinì, K. Reimann, *et al.*, “Two-phonon quantum coherences in indium antimonide studied by nonlinear two-dimensional terahertz spectroscopy,” *Phys. Rev. Lett.* **116**(17), 177401 (2016).
11. S. Houver, L. Huber, M. Savoini, *et al.*, “2d thz spectroscopic investigation of ballistic conduction-band electron dynamics in InSb,” *Opt. Express* **27**(8), 10854–10865 (2019).
12. F. Mahmood, D. Chaudhuri, S. Gopalakrishnan, *et al.*, “Observation of a marginal Fermi glass,” *Nat. Phys.* **17**(5), 627–631 (2021).
13. S. Pal, N. Strkalj, C.-J. Yang, *et al.*, “Origin of terahertz soft-mode nonlinearities in ferroelectric perovskites,” *Phys. Rev. X* **11**(2), 021023 (2021).
14. H.-W. Lin, G. Mead, and G. A. Blake, “Mapping LiNbO₃ phonon-polariton nonlinearities with 2D THz-THz-Raman,” *Phys. Rev. Lett.* **129**(20), 207401 (2022).
15. Z. Zhang, F. Y. Gao, Y.-C. Chien, *et al.*, “Terahertz-field-driven magnon upconversion in an antiferromagnet,” *Nat. Phys.* **20**(5), 788–793 (2024).
16. Z. Zhang, F. Y. Gao, J. B. Curtis, *et al.*, “Terahertz field-induced nonlinear coupling of two magnon modes in an antiferromagnet,” *Nat. Phys.* **20**(5), 801–806 (2024).
17. L. Luo, M. Mootz, J. H. Kang, *et al.*, “Quantum coherence tomography of light-controlled superconductivity,” *Nat. Phys.* **19**(2), 201–209 (2023).
18. A. Liu, D. Pavicevic, M. H. Michael, *et al.*, “Probing inhomogeneous cuprate superconductivity by terahertz Josephson echo spectroscopy,” (2023).
19. M.-J. Kim, S. Kovalev, M. Udina, *et al.*, “Tracing the dynamics of superconducting order via transient terahertz third-harmonic generation,” *Sci. Adv.* **10**(11), eadi7598 (2024).
20. T. G. H. Blank, K. A. Grishunin, K. A. Zvezdin, *et al.*, “Two-dimensional terahertz spectroscopy of nonlinear phononics in the topological insulator MnBi₂Te₄,” *Phys. Rev. Lett.* **131**(2), 026902 (2023).
21. S. Mukamel, *Principles of Nonlinear Optical Spectroscopy* (Oxford University Press, 1999).
22. P. Hamm and M. Zanni, *Concepts and Methods of 2D Infrared Spectroscopy* (Cambridge University Press, 2012).
23. A. G. Salvador, P. E. Dolgirev, M. H. Michael, *et al.*, “Principles of 2D terahertz spectroscopy of collective excitations: the case of Josephson plasmons in layered superconductors,” (2024).
24. S.-J. Kim, B. J. Kang, U. Puc, *et al.*, “Highly nonlinear optical organic crystals for efficient terahertz wave generation, detection, and applications,” *Adv. Opt. Mater.* **9**(23), 2101019 (2021).
25. Q. Wu, M. Litz, and X. Zhang, “Broadband detection capability of ZNTE electro-optic field detectors,” *Appl. Phys. Lett.* **68**(21), 2924–2926 (1996).
26. A. Sell, A. Leitenstorfer, and R. Huber, “Phase-locked generation and field-resolved detection of widely tunable terahertz pulses with amplitudes exceeding 100 mv/cm,” *Opt. Lett.* **33**(23), 2767–2769 (2008).
27. R. Boyd, *Nonlinear Optics* (Academic Press, 2020).
28. M. Lorenc, M. Ziolk, R. Naskrecki, *et al.*, “Artifacts in femtosecond transient absorption spectroscopy,” *Appl. Phys. B* **74**(1), 19–27 (2002).